Deformation and dynamics of erythrocytes govern their traversal through microfluidic devices with a deterministic lateral displacement architecture

Wei Chien, Zunmin Zhang, Gerhard Gompper, and Dmitry A. Fedosov[a)]

AFFILIATIONS

Theoretical Soft Matter and Biophysics, Institute of Complex Systems and Institute for Advanced Simulation, Forschungszentrum Jülich, 52425 Jülich, Germany

[a)]**Author to whom correspondence should be addressed:** d.fedosov@fz-juelich.de

ABSTRACT

Deterministic lateral displacement (DLD) microfluidic devices promise versatile and precise processing of biological samples. However, this prospect has been realized so far only for rigid spherical particles and remains limited for biological cells due to the complexity of cell dynamics and deformation in microfluidic flow. We employ mesoscopic hydrodynamics simulations of red blood cells (RBCs) in DLD devices with circular posts to better understand the interplay between cell behavior in complex microfluidic flow and sorting capabilities of such devices. We construct a mode diagram of RBC behavior (e.g., displacement, zig-zagging, and intermediate modes) and identify several regimes of RBC dynamics (e.g., tumbling, tank-treading, and trilobe motion). Furthermore, we link the complex interaction dynamics of RBCs with the post to their effective cell size and discuss relevant physical mechanisms governing the dynamic cell states. In conclusion, sorting of RBCs in DLD devices based on their shear elasticity is, in general, possible but requires fine-tuning of flow conditions to targeted mechanical properties of the RBCs.

Published under license by AIP Publishing. https://doi.org/10.1063/1.5112033

I. INTRODUCTION

Sorting biological cells based on their intrinsic properties and the detection of a cell subpopulation with specific mechanical characteristics are important objectives directly relevant for a number of biomedical and clinical applications.[1–3] The capability of sorting erythrocytes or red blood cells (RBCs) based on changes in their elastic properties is relevant for several blood diseases and disorders, such as sickle-cell anemia and malaria.[4,5] Deterministic lateral displacement (DLD) microfluidic devices have demonstrated excellent and precise performance for size-based label-free separation of rigid spherical colloidal particles.[6–8] DLD devices employ a designed array of obstacles (or posts) sandwiched between two planar walls, arranged such that every row of posts is laterally shifted with respect to the previous row. Such a geometric arrangement leads to several laminar flow streams within the DLD device, where the fluid stream adjacent to a post (also called the first stream) passes under the following post[9,10] (see Fig. 1). The thickness β of the adjacent stream defines the critical size of the device

such that particles with a smaller size than 2β traverse the DLD device in a zig-zagging (ZZ) fashion, following the streamline with a nearly zero lateral displacement, while larger particles are bumped laterally by consecutive shifted posts, switching the flow lanes in a displacement (DP) mode. Recent studies[8,11–13] have also demonstrated the existence of a mixed mode for rigid spherical particles with a lateral displacement between the ZZ and DP modes. Thus, in this ratchetlike way, precise sorting of rigid spherical particles based on their size can be achieved.

DLD devices have also been applied to sorting biological cells.[14–19] The separation results are generally good when biological particles of interest possess significantly different sizes, such as erythrocytes and leukocytes in the blood, but are poor when targeted cell populations have overlapping sizes. In comparison to rigid spherical particles, biological cells are deformable and often have a nonspherical shape. For example, RBCs have a biconcave disklike shape and are subject to strong and dynamic deformations in fluid flow.[20–23] Therefore, biological cells deform in response to local fluid stresses in DLD devices, and thus, cannot be straightforwardly characterized
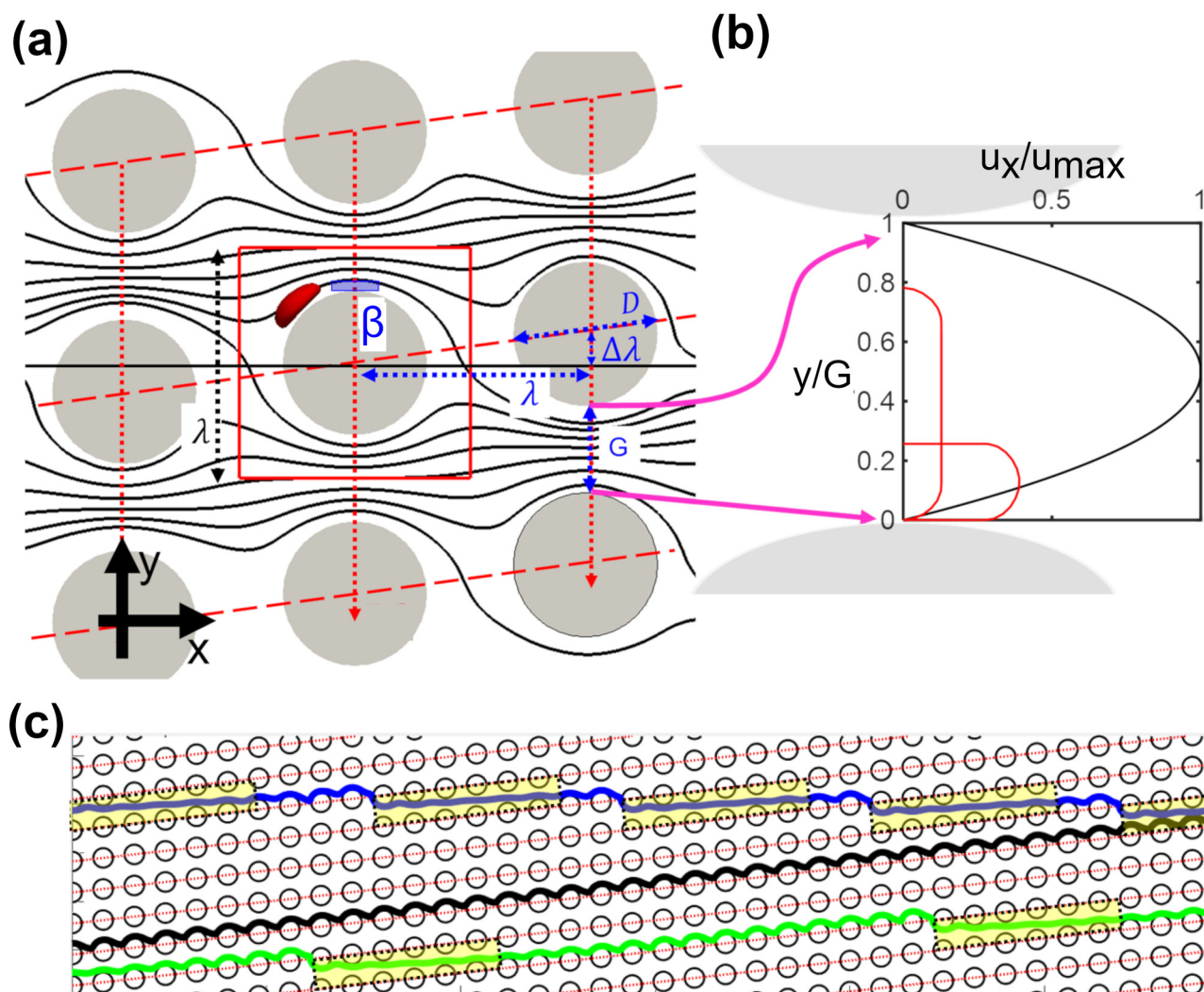
FIG. 1. Schematic of a DLD device and cell traversal through it. (a) Geometrical parameters of the device, including the post distance $\lambda = 35\,\mu$m, the gap size $G = 10\,\mu$m, and the row shift $\Delta\lambda$. The red square indicates the simulation domain. β shows the critical size of the device determined from the thickness of the first stream. (b) Schematic velocity profile within the gap between two posts (post size is drawn not to scale). The physical contours of a RBC are shown in red. (c) Illustration of several trajectories of a RBC within the DLD device with n = 8, representing displacement (DP) mode (black line), zig-zagging (ZZ) mode (blue line), and intermediate (IM) mode (green line). The boundaries of the device lanes are shown by the red dashed lines. The yellow stripes mark the portions of the RBC trajectories, where the RBC does not directly interact with the posts so that these portions are irrelevant for the selection of DP or ZZ motion.

by a fixed size.[16,24,25] Instead, the lateral displacement of biological cells in DLD devices can be characterized by an effective size, which is different from their undeformed size and depends on the cell's mechanical properties and local fluid-flow stresses within the device.

In the context of sorting RBCs, several studies[17,24,25] have considered "thin" DLD devices, for which the height h is smaller than the RBC diameter of $8\,\mu$m. In such devices, the rotational freedom of RBCs is constrained between the lower and upper walls, simplifying the cell dynamics within the device. Even though thin DLD devices have shown some sensitivity to RBC deformability,[17,24] they are prone to clogging due to frequent interactions of RBCs with the

walls. In contrast, "thick" DLD devices with $h > 8\,\mu$m allow for a much higher throughput, but do not put any restrictions on the RBC's orientation, yielding a more complex cell dynamics. An experimental study of RBC traversal through a thick DLD device has shown a poor sensitivity to RBC deformability,[25] because a RBC orients itself perpendicular to the shear plane, exposing its thickness ($\approx 2.8\,\mu$m) for sorting instead of its long diameter ($\approx 8\,\mu$m). However, a recent combined experimental and simulation investigation[16] has demonstrated RBC sorting in a thick DLD device based on the viscosity contrast $C = \eta_{in}/\eta_{out}$ between RBC cytosol and suspending medium, emphasizing the importance of

RBC dynamics in the device. Flipping dynamics of RBCs has also been hypothesized to play an important role in their traversal through DLD devices with I-shaped posts.[19] Furthermore, a recent numerical study suggests that sharp-edged DLD posts are advantageous for deformability-based RBC sorting, as they impose pronounced cell-deformation modes.[26] The importance of both RBC dynamics and deformation in DLD flow for deformability-based sorting demands a better understanding of the interplay between these two characteristics and their effect on sorting of RBCs based on their intrinsic properties.

To this end, we employ a thick DLD device with circular-shaped posts and investigate the sorting of RBCs based on their elastic properties at a viscosity contrast $C = 1$. We construct a mode diagram of RBC behavior for a wide range of membrane shear elasticities μ and row shifts $\Delta\lambda$, which allows us to characterize the dependence of the DP-ZZ transition on μ or the corresponding capillary number Ca. In particular, we identify three different regimes of RBC behavior depending on Ca. At low Ca, RBCs exhibit tumbling (TU) dynamics with small shape deformations, while at large Ca, RBCs generally show tank-treading (TT) dynamics with significant stretching in the flow direction. In the intermediate Ca regime, RBC dynamics is characterized by a superposition of TU and TT motion with strong and dynamic shape deformations. These dynamic states are qualitatively similar to those of RBCs in simple shear flow.[21–23,27,28] Interestingly, the DP-ZZ transition is a nonmonotonic and re-entrant function of Ca, which can be explained by an effective RBC size within the DLD device. As a result, we provide a link between the effective cell size and dynamic RBC behavior and identify the physical mechanisms involved.

The paper is organized as follows. The employed models and methods including simulation setup are described in Sec. II. Section III presents the mode diagram for a wide range of capillary numbers and a detailed analysis of dynamic RBC behavior in the DLD device. Finally, in Sec. IV, we summarize and discuss the simulation results and their importance for RBC sorting.

II. MODELS AND METHODS

In simulations, a coarse-grained RBC model[29–32] is employed and coupled to a mesoscopic representation of fluid flow by the smoothed dissipative particle dynamics (SDPD) method.[33–36] The simulation approach is similar to previous work,[16] where a good quantitative agreement between simulations and corresponding experiments has been achieved.

A. RBC membrane model

The cell membrane is modeled by a triangulated surface[29–31] with 1000 vertices, 1996 faces, and 2994 bonds to have a resolution around $0.4\,\mu\text{m}$ that is the average bond length. We use a RBC model with average size and shape (see Table I) characterized by an effective diameter $D_r = \sqrt{A/\pi}$ and reduced volume $v_r = 6V/(\pi D_r^3)$, where V is the cell volume and A is the surface area. Potential energies are applied to capture the mechanical properties of the membrane including the in-plane elastic energy, which mimics the elasticity of the spectrin network, the bending energy which represents bending rigidity of the lipid bilayer, and the constraints for area and volume which account for the

TABLE I. The standard parameters of a healthy RBC used in this study: the cell area A, cell volume V, cell diameter D_r, reduced volume v_r, bending rigidity κ, the shear modulus μ, and Föppl-von-Kármán number Γ.

A	$132.90\,\mu\text{m}^2$	κ	$70\,k_B\text{T}$
V	$90.21\,\mu\text{m}^3$	μ	$4.67\,\mu\text{N/m}$
D_r	$6.51\,\mu\text{m}$	Γ	681.5
v_r	0.62		

incompressibility of the lipid bilayer and inner cytosol, respectively.[29,30] This model has been shown to capture RBC deformation even in the nonlinear regime.[29,30,37] The mechanical properties quantified by the shear modulus μ and the bending rigidity κ are summarized in Table I. The dimensionless Föppl-von-Kármán number $\Gamma = \mu D_r^2/\kappa$ is chosen to mimic that of a healthy RBC.[38] The RBC model assumes a stress-free shape of the elastic network to be spheroidal with $v_r^{free} = 0.96$. Furthermore, we apply a homogeneous spontaneous curvature $\widetilde{c}_0$ characterized by the normalized curvature $c_0 = \widetilde{c}_0\,D_r/2 = 3$, following a previous numerical study.[39] The strengths of the total area, local area, and volume constraint coefficients (k_a, k_d, and k_v) are set large enough to restrict the total change in the surface area and volume to be within 5% for all simulated flow conditions.

B. Modeling fluid flow in a DLD device

The fluids inside and outside the cell are modeled by the smoothed dissipative particle dynamics (SDPD) method with angular momentum conservation.[34] SDPD is a particle-based hydrodynamics method that is obtained by a Lagrangian discretization of the Navier-Stokes equations[33–36] and includes consistent thermal fluctuations.[35] In SDPD, each particle represents a small fluid volume and interacts with other surrounding particles via pairwise soft potentials. The dynamic viscosity of a SDPD fluid is set directly as an input parameter. SDPD parameters are selected such that the simulated fluid can be considered incompressible[40] for Mach numbers $\text{Ma} = u_{max}/u_s < 0.01$, where u_{max} is the maximum flow velocity and u_s is the speed of sound.

The coupling between the SDPD fluid and the membrane particles is implemented by viscous friction through a dissipative force.[30] Bounce-back reflection of fluid particles is applied at the membrane triangles to impose membrane impenetrability. The viscosity of the internal fluid, η_{in}, is set to be the same as that of an external fluid, $\eta_{out} \equiv \eta_{in}$, so that the viscosity ratio $C = \eta_{in}/\eta_{out} = 1$. Solid walls are modeled by a layer of immobile SDPD particles, whose structure and density are identical to those of the SDPD fluid. Therefore, interactions between fluid and solid particles are the same as fluid-fluid interactions. The particle number density is set to $\rho = 9\,\mu\text{m}^{-3}$ to reasonably resolve fluid flow within $0.48\,\mu\text{m}$, which is comparable to the resolution of the membrane. In addition, a reflective boundary condition (similar to a hard-wall potential) is applied to fluid and membrane particles at solid surfaces and an adaptive shear force is added to fluid particles in the direction tangential to a solid surface in order to ensure no-slip boundary conditions.[41]

C. Simulation setup

Figure 1(a) shows a typical DLD geometry with cylindrical posts of circular cross section. The employed geometry is characterized by post distance $\lambda = 35\,\mu$m, post diameter D = 25 μm, gap size G = 10 μm, and row shift $\Delta\lambda$ that is varied. The corresponding geometric period of the DLD device is $n = \lambda/\Delta\lambda$. The height of the DLD device or the distance between two confining surfaces is set to $h = 10\,\mu$m such that a RBC has full rotational freedom within the device. The simulation domain contains a cube region with a single cylindrical post that is indicated by the red square in Fig. 1(a). In both flow (x) and gradient (y) directions perpendicular to the post axis, periodic boundary conditions are employed. However, for the periodic boundary in the x direction, a row shift $\Delta\lambda$ is introduced along the y direction to represent the shift of subsequent rows of posts. The flow is driven in the x direction by a constant body force applied to each fluid particle. In addition, an adaptive force is applied in the y direction to ensure no net flux in the flow-gradient direction.[8,16]

To characterize the flow stresses in comparison to cell deformation, the capillary number $Ca = \dot{\gamma}\eta D_r/\mu$ is employed with an average shear rate $\dot{\gamma} = u_{max}/G$, where u_{max} is the maximal value in the velocity profile captured from simulations without RBCs, as shown in Fig. 1(b). Ca is altered by changing the membrane shear modulus μ. Other mechanical parameters of a RBC (e.g., κ, k_a, k_d, and k_v) are also rescaled together with μ by the same factor so that the Föppl-von-Kármán number Γ remains fixed and the constraints of cell area and volume are consistent. Furthermore, the Mach number Ma and Reynolds number $Re = \rho G u_{max}/\eta < 0.3$ of the flow are unaffected by this variation of Ca. The capillary number of course also depends linearly on the flow rate (or applied pressure gradient) within the DLD device. We employ the definition of Ca based on the shear modulus, since μ is likely a dominant factor for RBC dynamics.[21] However, another capillary number $Ca_\kappa = \dot{\gamma}\eta D_r^3/\kappa$ based on the membrane bending rigidity may also affect RBC dynamics. Note that Ca and Ca_κ are related through the Föppl-von-Kármán number Γ that is kept constant in our investigation.

III. RESULTS

To characterize the lateral displacement of a RBC along the y direction, we compute an average lateral shift l_{ave} per row of posts from RBC trajectories as the ratio of the total lateral displacement of the RBC to the number of post rows it has traversed over the whole time of the simulation. In general, RBCs can have a very large number of different trajectories (or modes) in a DLD device depending on $\Delta\lambda$ and mechanical properties of the cells.[16,26] Therefore, a continuous displacement index $I_d = l_{ave}/\Delta\lambda$ is a convenient measure for distinguishing various types of RBC lateral displacements. For simplicity, all trajectories are classified into three groups, corresponding to different ranges of I_d. The motion of a RBC is classified as the DP mode whenever $I_d > 0.8$ [black trajectory in Fig. 1(c)]. Note that a perfect DP mode, for which the cell always remains within the same device lane [or between two red dashed lines in Fig. 1(c)], corresponds to $I_d = 1$, while for $I_d > 0.8$ some RBC trajectories may contain infrequent lane-swapping events. The class of ZZ modes is defined by $I_d < 0.2$, where the

RBC frequently switches device lanes [blue trajectory in Fig. 1(c)], and the neutral ZZ mode with zero net lateral displacement corresponds to $I_d = 0$. Note that slightly negative lateral displacements of the RBC with $I_d < 0$ are also possible.[16] Finally, trajectories with $0.2 \leq I_d \leq 0.8$ are classified as the intermediate (IM) mode [green trajectory in Fig. 1(c)]. The choice of boundaries for these classes is motivated by the condition that they should be close to the displacement indices $I_d = 0$ and $I_d = 1$, representing the classical, ideal ZZ, and DP modes. Commonly, the DP-ZZ transition occurs quite abruptly as a function of $\Delta\lambda$,[16,26] making the analysis of RBC trajectories nearly insensitive to the exact choice of these boundaries.

Recent simulations[16] of RBCs in a DLD device have shown that RBC trajectories are nearly deterministic and self-repeating at usual flow rates so that they possess a periodicity length characterized by a certain number of traversed post rows [e.g., see the ZZ trajectory in Fig. 1(c)]. For DP and ZZ modes defined above, the periodicity length of a RBC trajectory is generally quite short so that long simulation times are not necessary for a reliable estimation of I_d. In contrast, for IM modes, the periodicity length can be quite large, requiring very long simulations. As a rule of thumb, each simulation has been run so long that the RBC traverses at least $2n$ post rows. Several simulations near the DP-ZZ transition have been run even longer for a reliable calculation of I_d.

A. DLD mode diagram

By measuring I_d for various row shifts $\Delta\lambda$ and capillary numbers Ca, we can construct a DLD mode diagram for a single RBC, as shown in Fig. 2. We focus mainly on the transition between DP and ZZ modes, which can be characterized by a small range of $\Delta\lambda$ values for every fixed Ca, because it represents a good separatrix for sorting. Interestingly, this transition or a corresponding critical shift $\Delta\lambda_c$ (marked schematically by the red dashed line in Fig. 2) is a complex function of Ca. For $Ca \leq 0.01$, $\Delta\lambda_c$ varies within the range 3.2–4.0 μm and reaches a maximum at $Ca = 0.01$. For $0.01 < Ca < 0.3$, the critical shift first decreases to a minimum value around $Ca \cong 0.05$ and then increases again for larger Ca values. Finally, for $Ca \geq 0.3$, $\Delta\lambda_c$ continues to slightly increase but seems to level off at large Ca values. In fact, the regions of Ca, in which $\Delta\lambda_c$ has the strongest variations, are the most interesting for deformability-based sorting, because cells with differing shear moduli would attain distinct traversal modes through the DLD device. Therefore, flow conditions within a DLD device have to be selected carefully and should be directly associated with the targeted mechanical properties of RBCs. Note that the range of capillary numbers in Fig. 2 covers about three orders of magnitude, representing a large range of RBC shear moduli or similarly a large range of flow rates within the DLD device.

Figure 3 shows the average RBC velocity u_{RBC} normalized by the average fluid velocity U_{ave} as a function of $\Delta\lambda$ and Ca. Interestingly, the transition between DP and ZZ modes is strongly correlated with u_{RBC}/U_{ave} such that this ratio is generally smaller than unity near the transition. This means that a RBC in the IM mode moves on average slower than the average flow velocity, while the DP and ZZ modes generally lead to $u_{RBC}/U_{ave} > 1$. In the IM mode, RBC often comes close to the stagnation point at the left-
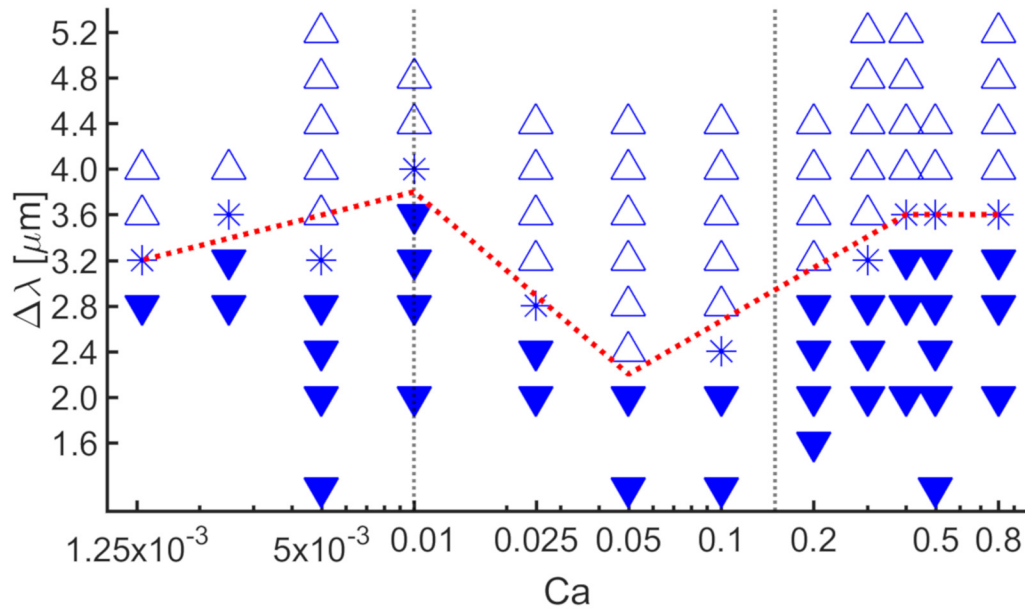
**FIG. 2.** DLD mode diagram as a function of *Ca* and Δλ. Different modes, including displacement (DP, solid triangles), intermediate (IM, * symbols), and zig-zagging (ZZ, hollow triangles) modes, are shown. The resolution in Δλ is 400 nm. The DP-ZZ transition or a corresponding critical shift $\Delta\lambda_c$ is indicated schematically by the red dashed line. l_d at each point is calculated for RBC traversal over at least $2n$ rows.

hand side of posts, where flow nearly vanishes. A similar behavior of RBCs has also been found in a thin DLD device, whose height is smaller than the RBC diameter.[24] Note that the width of the transition region with $u_{RBC}/U_{ave} < 1$ is larger for low *Ca* than for high *Ca* values.

B. Dynamic states of RBCs in DLD devices

Clearly, the dependence of $\Delta\lambda_c$ on capillary number *Ca*, marked schematically by the dashed line in Fig. 2, is due to RBC dynamics and deformation generated by the fluid stresses near the posts. To better understand the dependence of the DP-ZZ transition on *Ca*, we characterize the deformation and dynamics of RBCs by several quantities, see Fig. 4. These include the inclination angle θ and the tilt angle Φ [Fig. 4(a)], where θ is the angle between the cell's orientational vector *n* and the x axis within the x-y shear plane (i.e., projected onto the plane) and Φ is the angle between *n* and the x-y plane, characterizing the tilt of the RBC from the shear plane. Note that the orientational vector *n* is determined by the eigenvector of the inertia tensor corresponding to the smallest eigenvalue. Furthermore, we monitor the time-dependent motion of the membrane through a tank-treading angle θ_D measured in a reference frame attached to the eigenvectors of the inertia tensor for a material region initially located at the RBC dimple [Fig. 4(b)]. At the beginning of each simulation, we set $\theta_D|_{t=0} = 0$. Then, θ_D departs deviates from the initial value whenever the RBC membrane is forced into a tank-treading-like motion by fluid stresses. RBC deformation is characterized by the largest cell length *a* and

the relative lateral stretching $W_{eff} = bc/(b_0 c_0)$, where $a \geq b \geq c$ are calculated from the eigenvalues λ_i of the inertia tensor [Fig. 4(c)], with $a = \sqrt{5(\lambda_2 + \lambda_3 - \lambda_1)/2}$, $b = \sqrt{5(\lambda_3 + \lambda_1 - \lambda_2)/2}$, and $c = \sqrt{5(\lambda_1 + \lambda_2 - \lambda_3)/2}$. The biconcave rest shape of a RBC has $a_0 = 4.277 > b_0 = 4.272 > c_0 = 1.442\,(\mu m)$. Even though W_{eff} is mainly intended to describe the lateral width of the RBC near the posts, it can also be used to distinguish different types of RBC deformation within DLD devices.
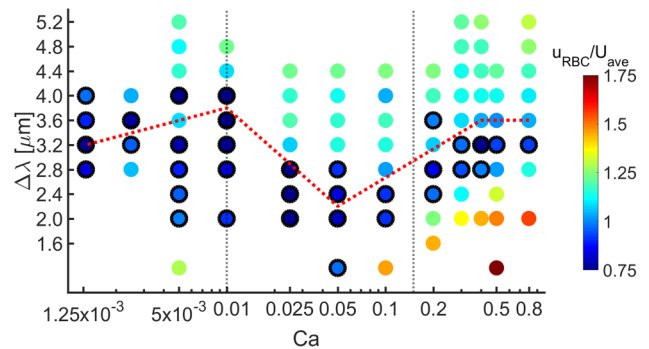
FIG. 3. Color map of RBC velocity u_{RBC} normalized by the average flow velocity U_{ave} as a function of *Ca* and Δλ. The black circles mark the conditions for which the ratio u_{RBC}/U_{ave} is smaller than unity. The DP-ZZ transition or a corresponding critical shift $\Delta\lambda_c$ is indicated schematically by the red dashed line.
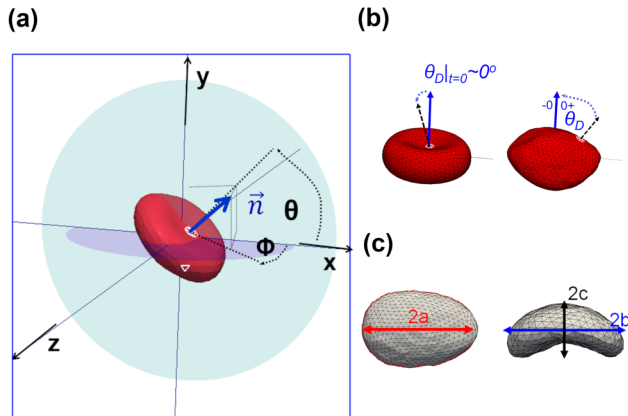
FIG. 4. Different quantities to characterize dynamical states of a RBC. (a) Cell orientation described by the inclination angle θ with respect to the x axis within the x-y plane (flow-gradient plane) and the tilt angle Φ from the x-z plane. The cell's orientational vector **n** is the symmetric axis of the shape drawn in blue. (b) Membrane motion characterized by a tank-treading angle θ_D. The white patch denotes a moving material region whose initial position corresponds to the cell's dimple and the orientational vector **n** is marked by the blue arrow. (c) Deformation of a RBC characterized by its largest length a and the relative lateral stretching $W_{eff} \equiv bc/(b_0 c_0)$, where b and c represent the lateral sizes of the RBC.

1. RBCs in a displacement mode

Large portions of ZZ and IM trajectories are not very important for the determination of lane crossing, as marked with yellow stripes in Fig. 1(c). They are identical and have essentially the same length. The RBC just flows along the stream within a single device lane without direct interaction with the posts. The cell approaches the post surface eventually, and the interaction between the RBC and the post surface is what matters, but it occurs less frequently in ZZ and IM modes than in the DP mode. Thus, we focus on the dynamics in DP, where the cell is locked in a certain device lane and repeatedly collides with the circular posts.

Along a DP trajectory, RBCs experience periodic and nonuniform local shear stresses, which are generally largest near the posts. Therefore, RBCs in the DP mode are subject to a periodic stretching and relaxation process in DLD flow, depending on the flow strength and RBC mechanical properties. In addition to RBC deformation, cell dynamics may affect the effective size. For example, in a linear shear flow, a RBC is known to exhibit tumbling (TU) at low Ca and tank-treading (TT) at high Ca for low viscosity contrasts $C \leq 3$.[21–23,27,42,43] The main mechanism of this transition is the shape memory of the cell's elastic network[28] and is related to an energy barrier for the TT motion of a RBC membrane.[42,43] Thus, fluid stresses are too small to overcome the energy barrier at low Ca, resulting in a TU motion of the RBC in simple shear flow. At high Ca, fluid stresses can overcome the elastic energy barrier, and RBC membrane sets into TT motion. For intermediate Ca between the TU and TT modes, there also exists a rolling motion[21,27] characterized by RBC orientation perpendicular to the shear plane, i.e., $\Phi \cong 90°$. In our DLD simulations, the rolling motion is nearly absent. The tilt angle relaxes to zero eventually for
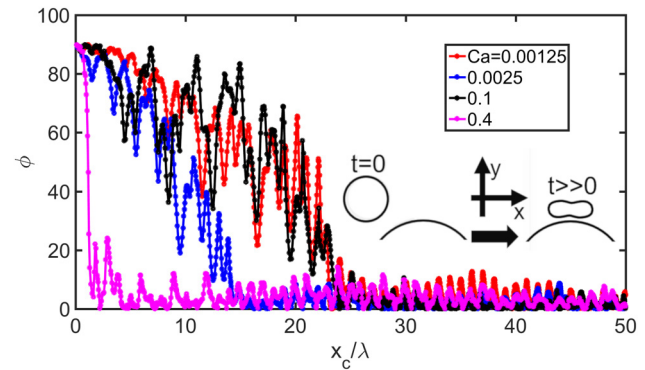
FIG. 5. Relaxation of the tilt angle Φ with an initial RBC orientation of $\Phi|_{t=0} = 90°$. In all simulations, the RBC attains a DP mode in a DLD device with $\Delta\lambda = 2\,\mu m$ and $\Delta\lambda/\lambda = 0.057$. The orientation change is schematically shown in the inset.

a wide range of Ca values, see Fig. 5. This is likely due to multiple collisions of RBCs with the posts in DP mode, which favors a cell's orientation with $\Phi \approx 0°$ for subsequent posts. Thus, we assume the initial cell orientation of $\Phi = 0°$ in all simulations.

2. Dynamic cell states at low capillary numbers

At low $Ca \in [0.001; 0.01]$, flow stresses are too weak to overcome the membrane's elastic barrier for tank-treading and the RBC tumbles similarly to a solid disk. In particular, the RBC slides along the curved post surfaces and tumbles after passing the top of the posts, as illustrated in Fig. 6(a) and confirmed quantitatively by the time evolution of the inclination angle θ that spans 360° [Fig. 6(c)]. The tilt angle remains close to $\Phi \approx 0°$ over the whole trajectory, independently of Ca. The tank-treading angle θ_D in Fig. 6(b) shows that the RBC membrane is subject to moderate oscillations whose amplitude becomes larger with increasing Ca. These oscillations indicate that the flow stresses initiate TT motion but are too small to impose full tank-treading. Figures 6(d) and 6(e) show that the RBC experiences small deformations with relative lateral stretching W_{eff} increasing by about 10% [Fig. 6(e)]. The increase in W_{eff} corresponds to the shape change from a biconcave shape with two dimples to a bowl shape with a single dimple, as illustrated in the inset of Fig. 6(a) and in Movie S1 in the supplementary material for $Ca = 0.01$. In conclusion, RBCs at low Ca exhibit TU dynamics with small membrane deformations in the DLD device, nearly independent of capillary number.

3. Dynamic cell states at intermediate capillary numbers

At intermediate $Ca \in [0.01; 0.15]$, a RBC in the DLD device with $\Delta\lambda = 2.0\,\mu m$ does not perform pure TU or pure TT motion, since neither θ_D nor θ span 360°, as shown in Figs. 7(c) and 7(d). The RBC motion is accompanied by strong and dynamic membrane deformations sensitive to Ca. A frequently occurring deformed shape is the trilobe (Tri)[21,44] [Figs. 7(a) and 7(b), Movies S2 and S3 in the supplementary material] with a relative lateral stretching
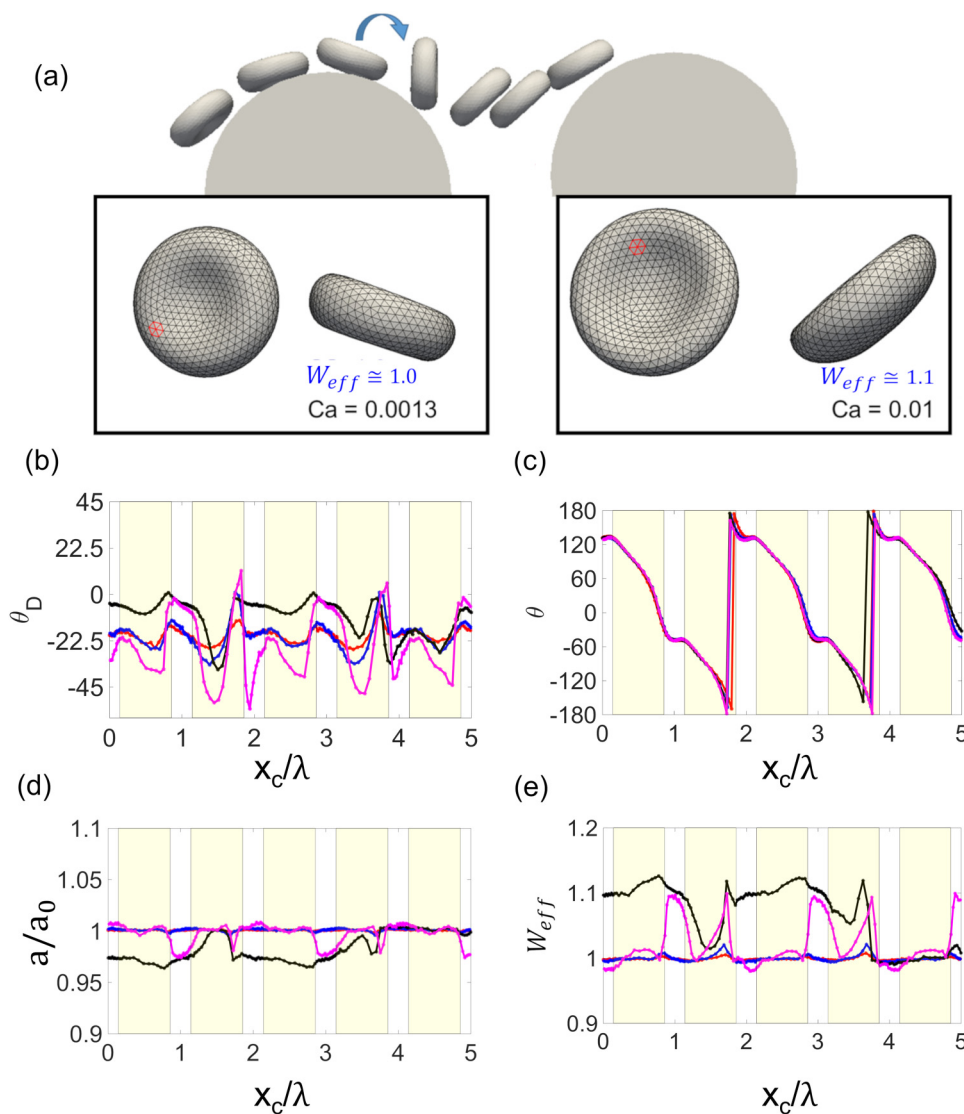
FIG. 6. Characteristics of tumbling-dominated displacement modes of RBCs in the DLD device with $\Delta\lambda = 2.0\,\mu m$ and $\Delta\lambda/\lambda = 0.057$. (a) Snapshots of tumbling-dominated motion at $Ca = 0.0013$ (see also Movie S1 in the supplementary material for $Ca = 0.01$). The cell shapes with $W_{eff} \approx 1$ and $W_{eff} = 1.1$ are shown. Evolution of (b) tank-treading angle θ_D, (c) inclination angle θ, (d) RBC stretching characterized by a/a_0, and (e) relative lateral stretching $W_{eff} = bc/(b_0 c_0)$. Colors represent capillary numbers: $Ca = 0.00125$ (red), 0.0025 (blue), 0.005 (black), and 0.01 (pink). Yellow shaded regions indicate the post locations.

larger than $W_{\text{eff}} \approx 1.2$. Similarly as in the low-Ca regime, $W_{\text{eff}} \approx 1.1$ represents a bowl shape, which also occurs when the RBC is located between two posts. Strong membrane deformations, especially for the trilobe shape, imply abrupt jumps of the cell's major axes, leading to discontinuous behavior of the angles θ_D and θ shown in Figs. 7(c) and 7(d). W_{eff} increases and a/a_0 decreases at the upstream side of the post when the RBC experiences increasing local shear rate while approaching the post top and then a recovery appears downstream, as shown in Figs. 7(e) and 7(f).

At intermediate Ca, the fluid stresses are comparable to the elastic barrier for membrane tank-treading. We find θ_D to be locked around $-60°$ before a discontinuous jump manifesting the effect of the elastic barrier occurs, as shown in Fig. 7(c). A critical Ca for going over the elastic barrier is between $Ca = 0.025$ of the tumbling trilobe [TU-Tri in Fig. 7(a)] and $Ca = 0.1$ of the tank-treading

trilobe [TT-Tri in Fig. 7(b)]. The recovery mechanism from high velocity gradients at the post top is schematically shown in Figs. 7(a) and 7(b); the membrane material point moves backward counterclockwise for TU-Tri while for TT-Tri it goes across $\theta_D = 90°$ and arrives at the dimple in the clockwise motion, following the flow.

4. RBC behavior at high capillary numbers

At high $Ca > 0.15$, the RBC membrane generally exhibits a TT motion, which is demonstrated by θ_D in Fig. 8(b), spanning over 360°. The inclination angle θ oscillates around an average value $\bar{\theta} \cong 112.5°$ [see Fig. 8(c)], which demonstrates that no TU motion occurs. Interestingly, the periodicity of θ_D (or membrane rotation) is not commensurate with the periodicity of DLD array structures. a/a_0 increases and W_{eff} decreases as the RBC
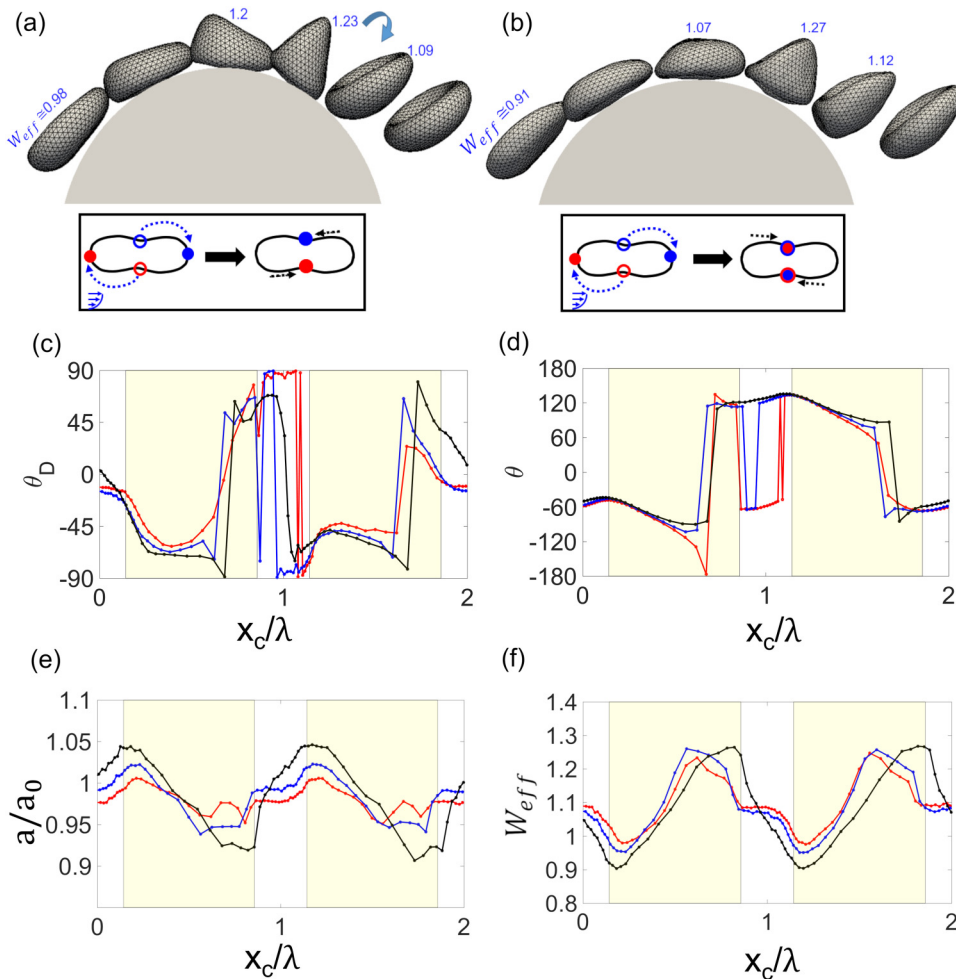
FIG. 7. RBC characteristics at the crossover between tumbling and tank-treading for intermediate $Ca \in [0.01; 0.15]$ in the DLD device with $\Delta\lambda = 2.0\,\mu m$ and $\Delta\lambda/\lambda = 0.057$. Snapshots for RBC dynamics at (a) $Ca = 0.025$ (Movie S2 in the supplementary material) and (b) $Ca = 0.1$ (Movie S3 in the supplementary material). The recovery processes of membrane material points are shown, where open circles indicate initial locations and solid circles correspond to intermediate locations under flow. Evolution of (c) θ_D, (d) θ, (e) a/a_0, and (f) $W_{eff} = bc/(b_0 c_0)$ for $Ca = 0.025$ (red), 0.05 (blue), and 0.1 (black). For a detailed description, see the caption of Fig. 6.

approaches the post top, where local shear rates are the highest, and these characteristics go in the reverse direction after passing the post top, as shown in Figs. 8(d) and 8(e).

At $Ca = 0.8$, a marker located initially inside one of the dimples of the biconcave RBC shape (i.e., in the middle of the cell in the z-direction) moves to one of the sides of a tank-treading RBC, corresponding to a minimum or maximum in the z-direction perpendicular to the flow x-y plane (Fig. 9). Such a drift of membrane material points in flow occurs only at very high Ca, as shown in Fig. 9. The same membrane drift has also been observed for RBCs in simple shear flow.[45,46] Another interesting observation is that the RBC does not directly touch post surfaces [Fig. 8(a)], as there is always a thin layer of fluid between the cell and the DLD posts (see Movie S4 in the supplementary material).

C. The link between the cell's dynamic states and its effective size

To link RBC dynamics and deformation to the DP-ZZ transition in Fig. 2, we aim to determine an effective cell size for sorting

from the complex dynamics. Figure 10 shows the deformation of the RBC as a function of Ca for DP modes. We find that the average shape of RBC remains the same below $Ca = 0.01$. For $Ca = [0.01; 0.15]$, we observe an increase of lateral effective stretching W_{eff} and a compression of the long axis a/a_0 along the stream. For $Ca > 0.2$, the RBC elongates and W_{eff} decreases. There is no direct correlation between the DP-ZZ transition boundary (or $\Delta\lambda_c$) and W_{eff}.

The key particle size to distinguish between DP and ZZ modes for deformable particles should be determined near the post top in relation to the width of the first stream. This has been demonstrated for RBCs in thin DLD devices with $h = 4.8\,\mu m$[24] and for DNA molecules in nano-DLD devices.[47] Following this idea, we calculate the maximum distance d_{far} between the RBC outer membrane surface and the post surface near the post top, as shown in Fig. 11(a). Indeed, the dependence of d_{far} on Ca exhibits a good functional resemblance with the DP-ZZ transition or $\Delta\lambda_c$ (marked by the red dashed line in Fig. 2). To illustrate directly that d_{far} and $\Delta\lambda_c$ are strongly correlated, Fig. 11(c) presents the mode diagram as a function of Ca and the double thickness 2β of the first stream,
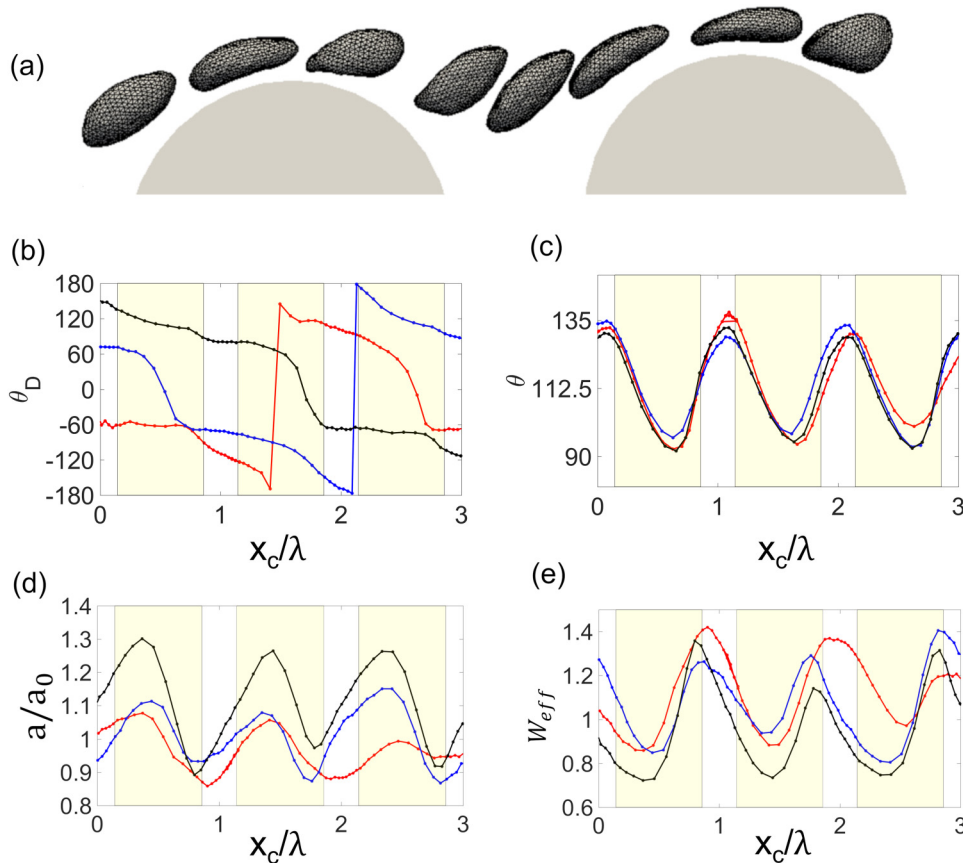
FIG. 8. Cell characteristics in a tank-treading dominated regime for high $Ca > 0.15$ in the DLD device with $\Delta\lambda = 2.0\,\mu$m and $\Delta\lambda/\lambda = 0.057$. (a) Snapshots for tank-treading dominated RBC dynamics at $Ca = 0.4$ (see also Movie S4 in the supplementary material). Evolution of (b) θ_D, (c) θ, (d) a/a_0, and (e) W_{eff} for $Ca = 0.2$ (red), 0.4 (blue), and 0.8 (black). For a detailed description, see the caption of Fig. 6.

which defines the critical size of a DLD device and is computed from simulations for various $\Delta\lambda$ without the cell (see Fig. S1 in the supplementary material). The correspondence between d_{far} and $\Delta\lambda_c$ in Fig. 11(c) is very good, confirming that the effective RBC size near the post top determines its traversal mode through the

device. Furthermore, the red dotted lines in Fig. 11(c) indicate the range of sizes between $2\beta_{min} = 2.9\,\mu$m (for $\Delta\lambda = 2.4\,\mu$m) and $2\beta_{max} = 3.9\,\mu$m (for $\Delta\lambda = 4.0\,\mu$m), which fully encloses the effective sizes d_{far} generated by RBC dynamics. Only the DP mode
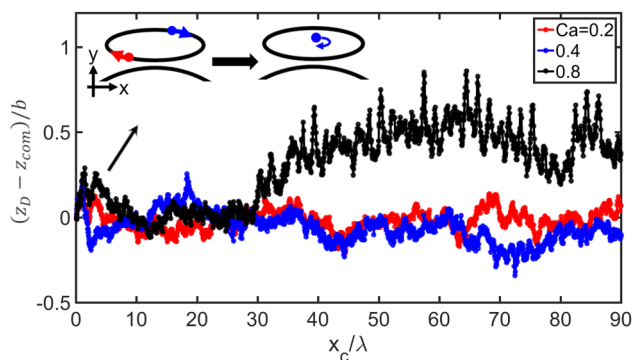
FIG. 9. The lateral drift of the membrane in the z-direction for $Ca = 0.8$ (black) with relative membrane motion schematically shown. For $Ca = 0.2$ (red) and 0.4 (blue), no lateral drift occurs.
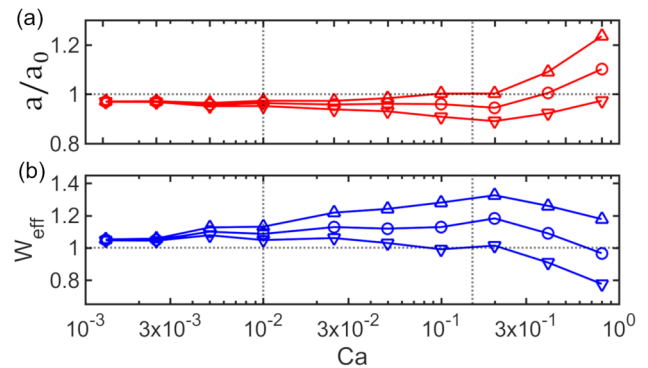
FIG. 10. Deformation of a RBC for DP modes with $\Delta\lambda = 2.0\,\mu$m. Average (O), maximum ($\triangle$), and minimum (∇) stretching a/a_0 (a) and effective lateral stretching W_{eff} (b) of RBC from simulations with a cell displacement larger than $2n\lambda$ in the x direction.
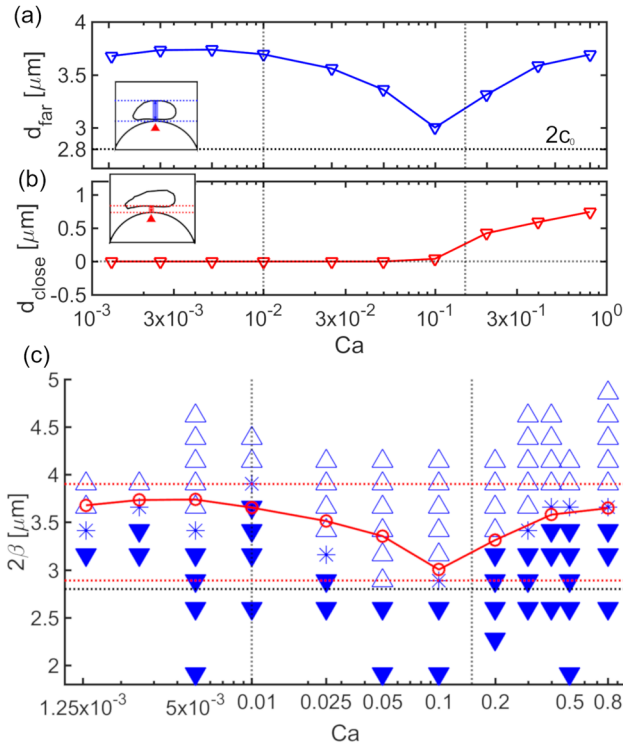
FIG. 11. Critical lengths estimated from DP modes with $\Delta\lambda = 2.0\,\mu m$ and $\Delta\lambda/\lambda = 0.057$. (a) The maximal distance d_{far} between the RBC membrane and the post surface near the post top, enclosed by the blue dashed lines in the inset. The black dotted line indicates the thickness $2c_0$ of an undeformed RBC. (b) The closest distance d_{close} between the RBC membrane and the post surface near the post top, as shown in the inset. Both d_{far} and d_{close} are calculated over at least $2n$ post rows. (c) The mode diagram as a function of Ca and the double thickness 2β of the first stream (see Fig. S1 in the supplementary material) obtained from simulations without a RBC. The red circles connected by a solid line represent the maximal distance d_{far}. The red dotted lines mark the double thickness of the first stream $2\beta_{min} = 2.9\,\mu m$ (at $\Delta\lambda = 2.4\,\mu m$) and $2\beta_{max} = 3.9\,\mu m$ (at $\Delta\lambda = 4.0\,\mu m$).

is present for $2\beta < 2\beta_{min}$ and only the ZZ mode for $2\beta > 2\beta_{max}$. Interestingly, $2\beta_{min}$ is larger than the thickness $2c_0 = 2.8\,\mu m$ of a RBC at rest. Therefore, the classical DLD explanation of particle separation through a critical size is still valid here.

At low $Ca \leq 0.01$, the TU dynamics of the RBC increases the effective thickness of the cell. This is illustrated well in Fig. 6(a), where the RBC displays a flipping motion already at the top of the circular post. The clockwise flipping motion is against the first stream and along the outer streams, which favors the displacement mode. The flipping mechanism originates from a sterical collision between the RBC and the post which explains the fluctuating values of I_d captured in Fig. 2.

At high $Ca > 0.15$, d_{far} increases as Ca increases [see Fig. 11(a)], even though W_{eff} decreases [see Fig. 10(b)]. Here, another physical mechanism plays an important role, since a thin fluid layer is observed between the RBC and DLD posts in

Fig. 8(a). To quantify the thickness of the fluid layer separating the RBC membrane and the DLD post surface, Fig. 11(b) displays the smallest width d_{close} of the fluid layer. For $Ca > 0.1$, d_{close} monotonically increases as a function of Ca, which is the main reason for an increase in d_{far} in Fig. 11(a). Note that the distance $d_{close} > 0$ is not a consequence of the flow field in the DLD device, because the local flow near the post is partially directed toward post surfaces due to a positive row shift, forcing RBCs toward the posts. Thus, there exists a force which pushes RBCs away from the posts and leads to a nonzero d_{close} at large Ca. Since there are no external forces involved, this force must arise from hydrodynamic interactions between the RBC and post surfaces, which is generally referred to as a lift force.[48,49] Another contribution may be the slow draining of the fluid from the gap, when the RBC is pressed against the post.

In the intermediate regime, a minimal effective size appears. For $Ca \in [0.01,\ 0.075)$, the RBC becomes more compressed as Ca increases. The compression reduces the extension away from the first stream and the destructive flipping effect mentioned above [see Fig. 7(a)] and implies a reduction of the effective size. At higher $Ca \in (0.075,\ 0.15]$, the contribution of partial TT motion becomes noticeable. This is due to the passing of the elastic barrier which enhances tank-treading even when the RBC experiences decreasing local shear rates, as it moves away from the post top [see Fig. 7(b)]. A tank-treading RBC experiences a significant hydrodynamic lift force due to hydrodynamic interactions with the posts, which leads to an increase in the effective size as Ca increases.

IV. SUMMARY AND DISCUSSION

We have demonstrated a potential DLD device which can probe shear elasticity of RBCs by tuning $\Delta\lambda$ from $2.4\,\mu m$ to $3.6\,\mu m$. The design of DLD devices with this range of $\Delta\lambda$ is realistic and has been realized in modern microfluidics.[16,25] Our design with $\lambda = 35\,\mu m$, $D = 25\,\mu m$, and $G = 10\,\mu m$ has larger posts and smaller gaps than the device in Ref. 25 with $\lambda = 32\,\mu m$, $D = 20\,\mu m$, and $G = 12\,\mu m$, which provides a more parabolic velocity profile[7] with lower velocity gradients near post surfaces under the same pressure drop. This helps enhance the sorting contrast at different Ca, originating from the cell dynamics triggered near the post surface.

The detailed analysis of RBC deformation and dynamics demonstrates the complexity of cell behavior in a DLD device with circular post shape. Three different regimes have been identified. At low $Ca \leq 0.01$, the RBC exhibits TU dynamics with orientation changes and small deformations. At intermediate $0.01 < Ca \leq 0.15$, fluid stresses are large enough to induce partial TT motion of the membrane. As a result, the RBC shows a mixture of both TU and TT dynamics and experiences strong membrane deformations. At high $Ca > 0.15$, the cell attains TT motion. RBC dynamics in the DLD device is qualitatively similar to that in simple shear flow, where cell tumbling at low shear rates and tank-treading at high shear rates for low viscosity contrasts C are observed.[21,28,42,43] The TU-TT transition is governed by the shape memory of a RBC,[28] which imposes an elastic energy barrier for TT motion.[42,43]

The critical $\Delta\lambda_c$ at the DP-ZZ transition varies with Ca and cannot be simply described by the thickness of RBC shape in equilibrium. Instead, the dependence of $\Delta\lambda_c$ on Ca can be attributed to

an effective RBC size, as the cell passes the top of posts. In fact, the effective cell size in the DLD device is larger than the thickness of the biconcave equilibrium shape for all Ca values. At low Ca, the RBC's effective size is governed by its flipping motion near the post top. At intermediate Ca, RBC deformations result in a decrease in the effective size, but this decrease stops when fluid stresses overcome the elastic barrier for membrane tank-treading. The elastic restoring force enhances tank-treading after this critical point and hydrodynamics lifting becomes important; thus, $\Delta\lambda_c$ begins to increase. At high Ca, the lift force increases, but the lateral cell size begins to decrease, resulting in a minor increase of $\Delta\lambda_c$. We expect that $\Delta\lambda_c$ at high Ca will reach a plateau since cell stretching nearly saturates at very high shear rates.

From the practical point of view, significant changes in $\Delta\lambda_c$ as a function of Ca are most interesting, as they allow the achievement of considerable contrasts in the lateral displacement of cells with distinct mechanical properties. For example, in the intermediate range of $0.01 < Ca \leq 0.1$, a choice of $\Delta\lambda \approx 2.6\,\mu m$ should allow the separation of softer and stiffer RBCs representing different Ca values. Similarly, the range of $0.1 < Ca \leq 0.4$ is also characterized by a significant increase of $\Delta\lambda_c$ as a function of Ca, which can be exploited for sorting based on RBC elastic properties. However, it is important to emphasize that a careful selection of flow properties (e.g., flow rate, device geometry) is necessary in order to achieve efficient deformability-based sorting. Furthermore, the selected flow properties need to fit well the targeted elastic characteristics of RBCs, as both affect the capillary number.

Changes in Ca in our simulations have been performed by altering the shear elasticity μ of RBC membrane. Another property that directly affects Ca is the flow rate in the DLD device which has been kept constant in all simulations. The assumption that Ca is the main governing parameter that controls RBC traversal through a DLD device implies the equivalence of flow stresses and cell elasticity such that the dependence of $\Delta\lambda_c$ on Ca in Fig. 2 would also reflect a change in flow rate. A recent two-dimensional simulation study[26] of RBC behavior in DLD devices with sharp-edged posts has tested the universality of capillary number as the dominant control parameter. The main conclusion of that study is that moderate changes in flow rates and RBC elastic properties are nearly equivalent and provide comparable results for RBC traversal through a DLD device, while overall the equivalence of flow stresses and cell elasticity reflected in Ca is at most qualitative. A similar conclusion about the universality of Ca as a control parameter is also expected here. Therefore, the capillary number is probably not the only dimensionless parameter that determines RBC behavior in DLD devices. Possible reasons for this complexity are nonlinear deformation and relaxation of the cell and intricate flow field and distribution of local stresses. Furthermore, in 3D there is another capillary number Ca_κ based on the membrane bending rigidity, which may also influence RBC behavior in DLD devices.

Finally, it is important to discuss the limitations of our simulation study. The mode diagram in Fig. 2 represents RBC behavior in the DLD device at a viscosity contrast $C = 1$ between the suspending medium and RBC cytosol. Note that under physiological conditions, the viscosity contrast is $C \approx 5$. In the regime of low Ca, we expect that a RBC with $C = 5$ would have a similar TU behavior as the RBC with $C = 1$. However, at high shear rates, deformation and dynamics of RBCs strongly depend on the viscosity contrast[21,44] such that the dependence of $\Delta\lambda_c$ at high enough Ca is likely to be different for $C = 5$ in comparison to that for $C = 1$. Nevertheless, Fig. 2 should represent well the behavior of RBCs with $C \leq 2$ in the investigated DLD device because RBC dynamics in simple shear flow is independent of viscosity contrast in this regime.[21] Furthermore, the RBC model employed in this study has not included membrane viscosity. Several recent simulation studies about RBC behavior in DLD devices,[16] in microchannel flow,[50] and in simple shear flow,[21] in which the membrane viscosity has been omitted, quantitatively reproduce corresponding experimental observations, suggesting that moderate membrane viscosity only weakly affects the behavior. Therefore, we expect only minor changes in the mode diagram in Fig. 2 for a nonzero membrane viscosity. Another limitation is that only the variation in shear modulus has been considered, while RBCs possess some variability in size and other mechanical properties such as bending rigidity. The variability in cell size is expected to have a moderate effect on the DP-ZZ transition, since RBCs expose their smallest size (i.e., thickness) due to cell orientation with $\Phi \approx 0°$ in the DLD device, and the variation in RBC thickness is not very large. Even though RBC shear elasticity is mainly responsible for the rich behavior of RBCs in simple shear flow,[21] the influence of membrane bending rigidity and of the stress-free shape on the DP-ZZ transition needs to be investigated in the future.

SUPPLEMENTARY MATERIAL

See the supplementary material for the double thickness 2β of the first stream as a function of $\Delta\lambda$ (Fig. S1) and four movies (Movies S1–S4), illustrating different RBC dynamics and deformation in DLD devices.

ACKNOWLEDGMENTS

REFERENCES

[1]G. Bao and S. Suresh, Nat. Mater. **2**, 715–725 (2003).

[2]D. Di Carlo, J. Lab. Autom. **17**, 32–42 (2012).

[3]M. Antfolk and T. Laurell, Anal. Chim. Acta **965**, 9–35 (2017).

[4]Y. Zhang, C. Huang, S. Kim, M. Golkaram, M. W. Dixon, L. Tilley, J. Li, S. Zhang, and S. Suresh, Proc. Natl. Acad. Sci. U.S.A. **112**, 6068–6073 (2015).

[5]D. A. Fedosov, Drug Discov. Today Dis. Models **16**, 17–22 (2015).

[6]L. R. Huang, E. C. Cox, R. H. Austin, and J. C. Sturm, Science **304**, 987–990 (2004).

[7]J. McGrath, M. Jimenez, and H. Bridle, Lab Chip **14**, 4139–4158 (2014).

[8]Z. Zhang, E. Henry, G. Gompper, and D. A. Fedosov, J. Chem. Phys. **143**, 243145 (2015).

[9]D. W. Inglis, J. A. Davis, R. H. Austin, and J. C. Sturm, Lab Chip **6**, 655–658 (2006).

[10]B. R. Long, M. Heller, J. P. Beech, H. Linke, H. Bruus, and J. O. Tegenfeldt, Phys. Rev. E **78**, 046304 (2008).

[11]R. Vernekar, T. Krüger, K. Loutherback, K. Morton, and D. Inglis, Lab Chip **17**, 3318–3330 (2017).

[12]S. C. Kim, B. H. Wunsch, H. Hu, J. T. Smith, R. H. Austin, and G. Stolovitzky, Proc. Natl. Acad. Sci. U.S.A. **114**, E5034–E5041 (2017).

[13]T. Kulrattanarak, R. G. van der Sman, Y. S. Lubbersen, C. G. Schroen, H. T. Pham, P. M. Sarro, and R. M. Boom, J. Colloid Interface Sci. **354**, 7–14 (2011).

[14]J. A. Davis, D. W. Inglis, K. J. Morton, D. A. Lawrence, L. R. Huang, S. Y. Chou, J. C. Sturm, and R. H. Austin, Proc. Natl. Acad. Sci. U.S.A. **103**, 14779–14784 (2006).

[15]S. H. Holm, J. P. Beech, M. P. Barrett, and J. O. Tegenfeldt, Lab Chip **11**, 1326–1332 (2011).

[16]E. Henry, S. H. Holm, Z. Zhang, J. P. Beech, J. O. Tegenfeldt, D. A. Fedosov, and G. Gompper, Sci. Rep. **6**, 34375 (2016).

[17]D. Holmes, G. Whyte, J. Bailey, N. Vergara-Irigaray, A. Ekpenyong, J. Guck, and T. Duke, Interface Focus **4**, 20140011 (2014).

[18]S. Ranjan, K. K. Zeming, R. Jureen, D. Fisher, and Y. Zhang, Lab Chip **14**, 4250–4262 (2014).

[19]K. K. Zeming, S. Ranjan, and Y. Zhang, Nat. Commun. **4**, 1625 (2013).

[20]D. A. Fedosov, M. Peltomaki, and G. Gompper, Soft Matter **10**, 4258–4267 (2014).

[21]J. Mauer, S. Mendez, L. Lanotte, F. Nicoud, M. Abkarian, G. Gompper, and D. A. Fedosov, Phys. Rev. Lett. **121**, 118103 (2018).

[22]K. Sinha and M. D. Graham, Phys. Rev. E **92**, 042710 (2015).

[23]D. Cordasco, A. Yazdani, and P. Bagchi, Phys. Fluids **26**, 041902 (2014).

[24]T. Krüger, D. Holmes, and P. V. Coveney, Biomicrofluidics **8**, 054114 (2014).

[25]J. P. Beech, S. H. Holm, K. Adolfsson, and J. O. Tegenfeldt, Lab Chip **12**, 1048–1051 (2012).

[26]Z. M. Zhang, W. Chien, E. Henry, D. A. Fedosov, and G. Gompper, Phys. Rev. Fluids **4**, 024201 (2019).

[27]J. Dupire, M. Socol, and A. Viallat, Proc. Natl. Acad. Sci. U.S.A. **109**, 20808–20813 (2012).

[28]T. Fischer, Biophys. J. **86**, 3304–3313 (2004).

[29]D. A. Fedosov, B. Caswell, and G. E. Karniadakis, Comput. Methods Appl. Mech. Eng. **199**, 1937–1948 (2010).

[30]D. A. Fedosov, B. Caswell, and G. E. Karniadakis, Biophys. J. **98**, 2215–2225 (2010).

[31]D. A. Fedosov, H. Noguchi, and G. Gompper, Biomech. Model. Mechanobiol. **13**, 239–258 (2014).

[32]H. Noguchi and G. Gompper, Proc. Natl. Acad. Sci. U.S.A. **102**, 14159–14164 (2005).

[33]P. Espanol and M. Revenga, Phys. Rev. E **67**, 026705 (2003).

[34]K. Müller, D. A. Fedosov, and G. Gompper, J. Comput. Phys. **281**, 301–315 (2015).

[35]A. Vazquez-Quesada, M. Ellero, and P. Espanol, J. Chem. Phys. **130**, 034901 (2009).

[36]M. Ellero and P. Español, Appl. Math. Mech. Engl. Ed. **39**, 103–124 (2017).

[37]M. Chen and F. J. Boyle, Mater. Sci. Eng. C **43**, 506–516 (2014).

[38]J. B. Freund, Annu. Rev. Fluid Mech. **46**, 67–95 (2014).

[39]Z. Peng, A. Mashayekh, and Q. Zhu, J. Fluid Mech. **742**, 96–118 (2014).

[40]D. Alizadehrad and D. A. Fedosov, J. Comput. Phys. **356**, 303–318 (2018).

[41]D. A. Fedosov and G. E. Karniadakis, J. Comput. Phys. **228**, 1157–1171 (2009).

[42]J. M. Skotheim and T. W. Secomb, Phys. Rev. Lett. **98**, 078301 (2007).

[43]M. Abkarian, M. Faivre, and A. Viallat, Phys. Rev. Lett. **98**, 188302 (2007).

[44]L. Lanotte, J. Mauer, S. Mendez, D. A. Fedosov, J. M. Fromental, V. Claveria, F. Nicoud, G. Gompper, and M. Abkarian, Proc. Natl. Acad. Sci. U.S.A. **113**, 13289–13294 (2016).

[45]D. Cordasco and P. Bagchi, Phys. Fluids **25**, 091902 (2013).

[46]Z. Peng and Q. Zhu, Soft Matter **9**, 7617–7627 (2013).

[47]B. H. Wunsch, S. C. Kim, S. M. Gifford, Y. Astier, C. Wang, R. L. Bruce, J. V. Patel, E. A. Duch, S. Dawes, G. Stolovitzky, and J. T. Smith, Lab Chip **19**, 1567–1578 (2019).

[48]M. Abkarian, C. Lartigue, and A. Viallat, Phys. Rev. Lett. **88**, 068103 (2002).

[49]S. Messlinger, B. Schmidt, H. Noguchi, and G. Gompper, Phys. Rev. E **80**, 011901 (2009).

[50]A. Guckenberger, A. Kihm, T. John, C. Wagner, and S. Gekle, Soft Matter **14**, 2032–2043 (2018).

[51]Jülich Supercomputing Centre, J. Large-Scale Res. Facil. **4**, A132 (2018).